

Research Article

Effects of Corn Stalk Fly Ash (CSFA) on the Mechanical and Deformation Properties of Cemented Coal Gangue Backfill

Tingye Qi ^{1,2} Haochen Wang ^{1,2} Guorui Feng ^{1,2} Xianjie Du ^{1,2} Zehua Wang ^{1,2}
and Shufeng Zhang^{1,2}

¹College of Mining Engineering, Taiyuan University of Technology, Taiyuan, China

²Shanxi Province Research Centre of Green Mining Engineering Technology, Taiyuan, China

Correspondence should be addressed to Guorui Feng; fgr09000@126.com

Received 17 October 2019; Accepted 17 January 2020; Published 11 February 2020

Guest Editor: Qiusong Chen

Copyright © 2020 Tingye Qi et al. This is an open access article distributed under the Creative Commons Attribution License, which permits unrestricted use, distribution, and reproduction in any medium, provided the original work is properly cited.

To reduce the amount of cement used in cemented coal gangue backfill (CCGB, a mixture of coal gangue, cement, fly ash, and water), mechanical and deformation properties of CCGB in which CSFA partially replaces the cement (0, 10, 20, 30, and 40 wt%) were studied. Compressive strength, acoustic emission during uniaxial loading, shear strength, and drying shrinkage were analysed. The compressive strength, shear strength, and drying shrinkage tests were performed at different curing times. The results showed that cemented coal gangue and corn stalk fly ash backfill (CGCAB) presented better performance, and the CGCAB with a 20% substitution rate had the best performance at day 28. Despite having the largest drying shrinkage value, 20% is the best choice for the substitution rate of CSFA. A 20% CSFA addition can enhance the bearing capacity of CGCAB and improve its failure mode, which is of great significance to support the upper overburden load and maintain the surface stability of the goaf.

1. Introduction

Backfilling mining is widely used to address surface subsidence caused by extensive mining, environmental pollution caused by coal gangue accumulation, and low coal recovery rate under buildings/railways/water-bodies [1, 2]. Cemented coal gangue backfill (CCGB) can be used to support overburden and prevent surface subsidence upon transportation through a pipeline to underground goaf [3–5]. CCGB can reuse solid waste and reduce landfill area, thus addressing environmental problems [6]. The CCGB for coal mine backfilling is an engineered mixture of coal gangue, fly ash, cement, and water; and the solids account for 75–85 wt% [7, 8]. In recent years, many scholars have conducted research on CCGB. Wu et al. [9] developed a coupling model to analyse the thermal-hydraulic-mechanical-chemical processes that occurred in CCGB. Yin et al. [10] proposed an electrochemical treatment to improve the early age strength and deformation characteristics of CCGB. Sun et al. [11] developed a test machine to test the creep disturbance effect of CCGB and established a creep

disturbance constitutive model of CCGB. However, CCGB still presents many practical issues such as insufficient materials [12], excessive cost [13], and low strength [14].

To solve the above problems, the introduction of corn stalk fly ash (CSFA) in the preparation of CCGB has been proposed. On one hand, corn is the main crop in China, and its yearly corn stalk production is significantly large [15, 16]. Moreover, corn stalks are transported to biomass power plants, and large amounts of CSFA are produced every year. On the other hand, CSFA has a certain pozzolanic activity and a large content of silica [17, 18]. If CSFA was introduced for use in the CCGB, it could reduce costs as partial cement replacement and address the high CSFA production. However, a few studies investigated the CSFA content influencing the physical, mechanical properties and micromechanism of CCGB and other cement-based materials.

The other biomass ashes, such as rice husk ash, have been studied as partial cement replacement in concrete [19]. In general, rice husk ash presents pozzolanic activity, and the incorporation of rice husk ash into concrete can improve its

mechanical properties, such as compressive strength and splitting tensile strength. Givi et al. [20] replaced cement by agro-waste rice husk ash at different proportions (5, 10, 15, and 20 wt%) and using two different average particle sizes (5 and 95 μm). According to the authors, cement can be replaced by up to 15% of the rice husk ash of 95 μm and 20% of the 5 μm ones for increased strength. The optimal strength of concrete was obtained when 5 μm particles replaced 10% of the cement. Raisi et al. [21] replaced cement with different proportions (5, 10, 15, and 20 wt%) of rice husk ash and prepared a control group using 100% cement. The compressive strength, splitting tensile strength, and elastic modulus of the concrete increased relative to the control group for 5 and 10% substitution at 28 days. Moreover, the group with a substitute content of 5% showed the maximum compressive strength, close to 50 MPa, at 28 days. This result was mainly attributed to the pozzolanic activity and physical filling ability peculiar to rice husk ash [22, 23].

The explanation for rice husk ash improving the strength of concrete is that rice husk ash can react with calcium hydroxide formed by cement hydration to form a dense structure of C-S-H gel, which makes the internal pores of concrete more compact. As the calcium ion concentration continues to decrease, the degree of cement hydration is again enhanced. In addition, the particle size of rice husk ash is also essential to enable the physical filling ability. Furthermore, the structure of rice husk ash particles determines that they can be used as a porous medium to store water [24]. In the early stages of cement hydration, rice husk ash particles absorb free water into their pores. At the later stage, the rice husk ash particles gradually release the internally stored water, which further develops the cement hydration process. However, some research scholars have concluded that the addition of rice husk ash to concrete reduces its compressive strength. This behaviour happens due to specific operations in the preparation of the concrete mixture which differ from the conventional operations. For example, Ismail and Waliuddin [25] adjusted the water-cement ratio to maintain the consistency of workability. Thus, the compressive strength decreased. Olutoge and Adesina [26] used high-early-strength Portland limestone cement and missed the pozzolanic reaction stage of rice husk ash. Therefore, the compressive strength was not effectively improved. Based on similar material compositions and engineering backgrounds, the direction of concrete provides good references for CCGB.

In this study, the cement in CCGB was replaced by CSFA at 0, 10, 20, 30, and 40 wt%, and the effects of substitution rates on the mechanical and deformation properties of cemented coal gangue and corn stalk fly ash backfill (CGCAB) were investigated. Upon analysing the test results, the optimal substitution rate for CGCAB mechanical and deformation performance was selected. The compressive strength, shear strength, and drying shrinkage tests were performed at different curing times. The acoustic emission detection was performed at day 28 under uniaxial loading conditions.

2. Materials and Methods

2.1. Raw Materials. The coal gangue used in the tests was obtained from the Tunlan coal mine, Taiyuan City, Shanxi Province. After being crushed, it was divided into fine aggregate (particle diameter smaller than 5 mm) and coarse aggregate (particle diameter of 5–15 mm). The cement used in the tests was ordinary Portland cement with a strength grade of 42.5, from Taiyuan Lionhead Cement Co., Ltd., Taiyuan City, Shanxi Province. The fly ash used was Class F and Class II fly ash from Hebei Woyang Mineral Products Trading Co., Ltd., Shijiazhuang City, Hebei Province. The CSFA used in the tests is from a power plant in Shijiazhuang City, Hebei Province. To reduce the impact of water content on the test results, the CSFA was first spread out and dried in an oven at 80°C for 24 h. Scanning electron microscopy (SEM) images of fly ash and CSFA are shown in Figure 1. The fly ash particles are in the form of glass beads, and the CSFA particles are irregular in shape and are mostly elongated. The main chemical composition and physical properties of various solid raw materials are shown in Table 1. The particle size distributions of CSFA and fly ash are shown in Figure 2, and the gradation of coal gangue determined in previous study [27] is shown in Table 2.

2.2. Specimen Preparation. As shown in Table 3, a control group (C0) and four variable groups (C1, C2, C3, and C4) were established. In all five groups, the amount of fine coal gangue was 285 kg/m³, the amount of coarse coal gangue was 665 kg/m³, and the amount of fly ash was 380 kg/m³. The amount of cement in the control group (C0) was 190 kg/m³, and, in the variable groups, CSFA replaced 10wt% (C1), 20wt% (C2), 30wt% (C3), and 40wt% (C4) of cement, respectively. For all mixtures, the mass concentration and water-binder ratio were kept constant at 83% and 0.55, respectively.

Following the Chinese standard GB/T 50080–2016 “Standard for test method of performance on ordinary fresh concrete,” the raw materials were mixed and stirred; then the mixtures were immediately poured into three types of cubic moulds: 100 mm × 100 mm × 100 mm (for compressive strength test and acoustic emission test), 70 mm × 70 mm × 70 mm (for shear strength test), and 100 mm × 100 mm × 515 mm (for drying shrinkage test). The fresh specimens were compacted using a vibrating table and then were covered with plastic sheets to prevent water loss. After 24 h, the specimens were removed from the moulds and placed in the curing room (temperature: 20 ± 2°C; humidity: 40 ± 5%) until the stable age. Before the start of each test, the surfaces of all test specimens were sanded with sandpaper.

2.3. Test Methods. The tests in this study were performed with three specimens each, and the final values were average values. The compressive strength test was performed in accordance with the Chinese standard GB/T 50081–2002 “Standard for test method of mechanical properties on ordinary concrete.” This test was performed within 3, 7, 14,

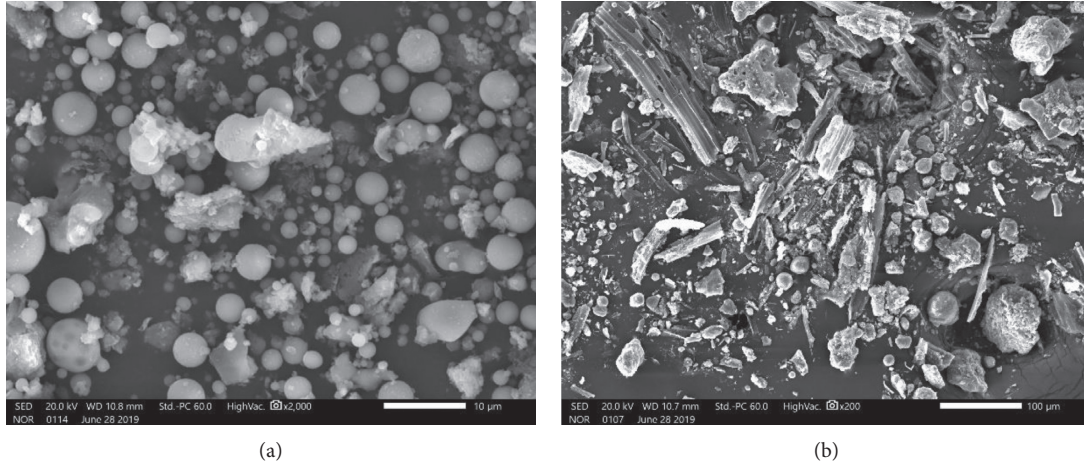


FIGURE 1: SEM images of supplementary cementitious materials: (a) fly ash and (b) corn stalk fly ash.

TABLE 1: Main chemical composition and physical properties of various solid raw materials.

	Coal gangue	Cement	Fly ash	CSFA
SiO ₂	28.46%	22.27%	52.42%	35.68%
Al ₂ O ₃	12.11%	5.59%	32.48%	6.10%
Fe ₂ O ₃	14.86%	3.47%	3.62%	7.40%
CaO	7.15%	65.90%	3.05%	9.98%
MgO	3.50%	0.81%	1.01%	2.60%
True density (g/cm ³)	2.31	3.10	2.09	2.13
Specific surface (m ² /kg)	—	349	415	222
Moisture content (%)	8.0	—	0.12	3.77

TABLE 2: Gradation of coal gangue [27].

Sieve size (mm)	Percent passing (%)
0.15	7.97
0.3	10.93
0.6	16.49
1.18	22.65
2.36	26.29
4.75	38.85
9.5	67.11
16	100

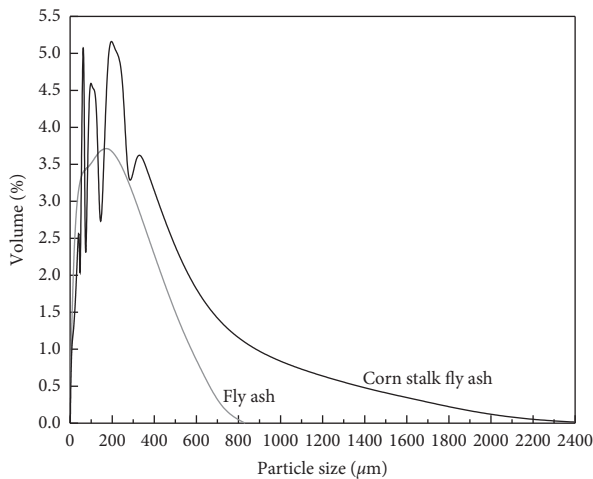


FIGURE 2: Particle size distribution of corn stalk fly ash and fly ash.

and 28 days after pouring. The pressure testing machine used a computer-controlled WDW-100 electronic universal testing machine with a full-scale specification of 100 kN, which can meet the failure load of the specimen to the fullest within 20–80% of the full scale of the press. For the compressive strength test, the loading rate was controlled at a displacement of 0.3 mm/min.

To grasp the failure characteristics of CGCAB under uniaxial loading conditions, acoustic emission test was used

for detection. The acoustic emission test under uniaxial loading conditions was performed within 28 days after pouring. The acoustic emission device adopted the DS5-8B acoustic emission device (Beijing Softland Times Scientific & Technology Co., Ltd.), with a preamplifier gain of 40 dB, a signal threshold of 40 dB, a sampling frequency of 25 kHz, a conversion accuracy of 16 bit, and a sampling rate of 5 million samples per channel. There were four signal receiving probes, which were arranged alternately on each side.

The shear strength test was performed in accordance with the Chinese standard DZ/T 0276.25–2015 “Regulation for testing the physical and mechanical properties of rock” (Part 25: Test for determining the shear strength of rock). The shear strength test was performed in the same day in comparison to the compressive strength test for the same mix proportion of the test specimens under the same curing age. The shear strength was measured through a wedge shear test, and the pressure testing machine used was the same as the one used for the compressive strength test. During the shear strength test, the selected angles of the shearing fixtures were 40°, 45°, 50°, and 55°. For the shear strength test, the loading rate was controlled at a displacement of 0.8 mm/min.

The drying shrinkage test was performed in accordance with the Chinese standard GB/T 50082–2009 “Standard for test methods of long-term performance and durability of ordinary concrete.” For the drying shrinkage test, the specimens were removed and placed on the concrete

TABLE 3: Mix proportions (kg/m³) of coal gangue backfilling materials.

Specimen	Substitution rate (wt%)	Fine gangue (0–5 mm)	Coarse gangue (5–15 mm)	Cement	Fly ash	CSFA	Water
C0	0	285	665	190	380	0	311.325
C1	10	285	665	171	380	19	311.325
C2	20	285	665	152	380	38	311.325
C3	30	285	665	133	380	57	311.325
C4	40	285	665	114	380	76	311.325

shrinkage meter after 3 days of curing. This test was performed at 1, 3, 7, 14, 28, 45, 60, 90, 120, and 180 days after curing. A concrete shrinkage meter (measuring gauge: 540 mm) and digital dial gauge (accuracy: 0.001 mm) were used.

3. Results and Discussion

3.1. Compressive Strength. The compressive strength of CGCAB at different ages and substitution rates is given in Figure 3. At day 3, the compressive strength showed a tendency to gradually decrease, and group C0 presented the highest compressive strength (2.4 MPa). At days 7 and 14, the compressive strength first increased and then decreased, and group C1 presented the highest compressive strengths (4.38 MPa and 6.25 MPa for days 7 and 14, respectively). At day 28, the compressive strength also first increased and then decreased. However, group C2 presented the highest compressive strength (9.69 MPa).

CSFA contains a large amount of oxides, such as silica and alumina, and it presents a certain pozzolanic activity. Thus, when CSFA is in contact with the calcium hydroxide formed by the hydration reaction of cement, a pozzolanic reaction occurs and calcium silicate hydrate (C-S-H) is formed [28]. C-S-H has an amorphous colloidal form with a dense structure that assists the increase of the pressure bearing capacity of CGCAB, thereby increasing its compressive strength. At early stages, the pozzolanic reaction has not yet entered the active stage. Therefore, if the substitution rate increases, the cement content decreases, and the compressive strength gradually decreases. When the curing time increases, especially at 28 days, the pozzolanic reaction gradually becomes effective. The CSFA addresses the absence of cementitious material and the compressive strength of CGCAB rapidly increases [29], which is especially clear when the substitution rate is 20%. For larger substitution rates, the water demand of CSFA causes the workability of CGCAB to decrease, thereby hindering the hydration and pozzolanic reactions, which cause the compressive strength to decrease [30, 31].

3.2. Acoustic Emission. It can be seen from Figure 4 that the strain corresponding to the stress peak is maintained within 0.02-0.03. When the substitution rate was 20%, the ring-down counts were the highest, which may be attributed to the increased production of C-S-H colloids with surface roughness and wrinkles [32, 33]. These colloids generate more transient elastic waves or stress waves by friction during uniaxial loading. The sources of acoustic

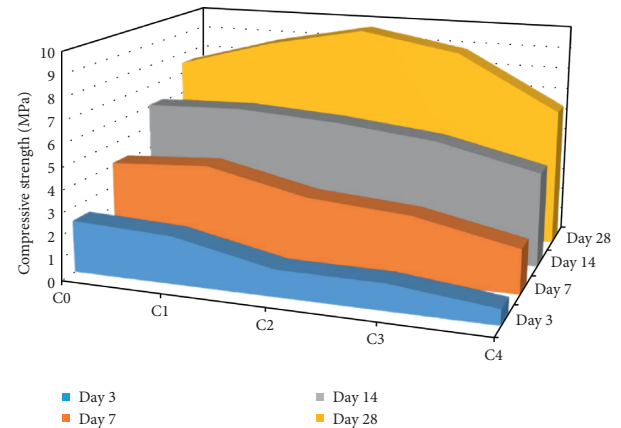
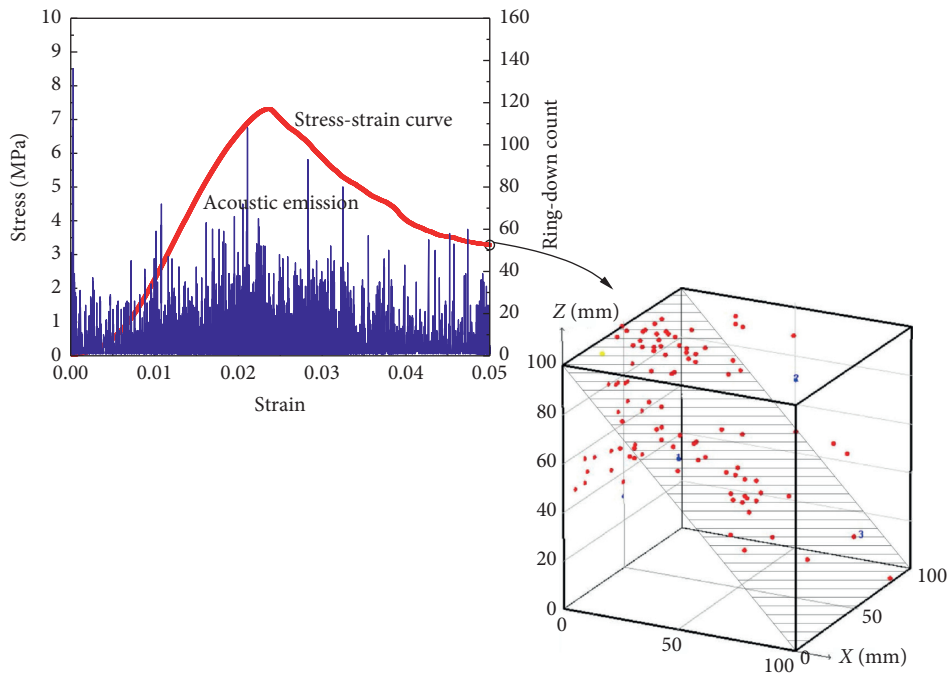


FIGURE 3: Trend of CGCAB compressive strength.

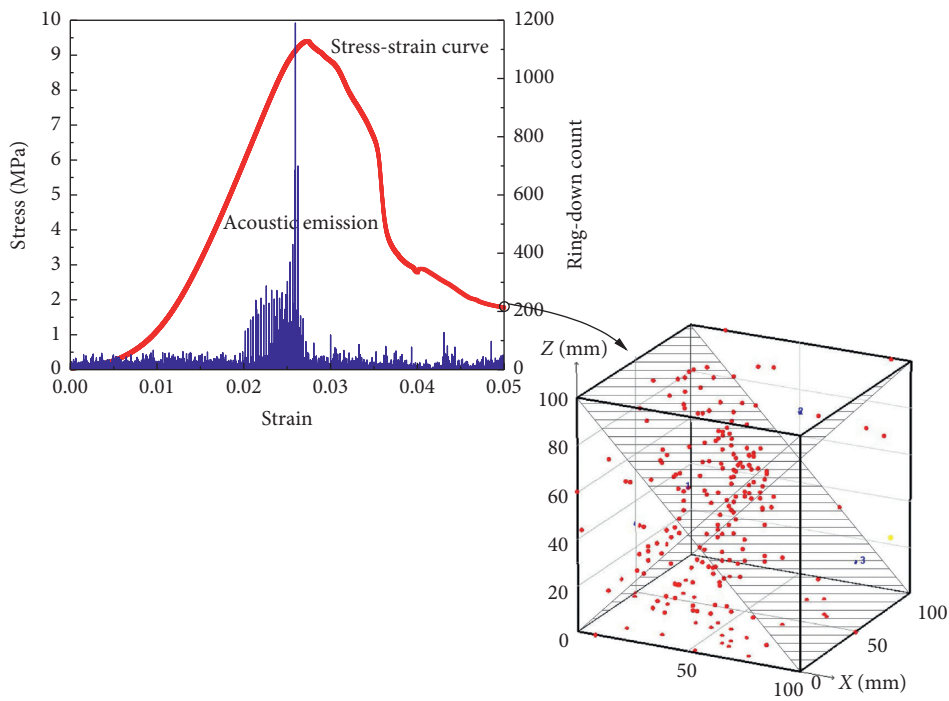
emissions inside the CGCAB include the friction between aggregate particles and the generation and expansion of cracks. Furthermore, the peak of the ring-down count generally occurred before the stress peak (after the yield point) and was in the unstable fracture development stage of CGCAB. These characteristics are established because the crack rapidly expands over a large area and the small fragments slid extensively during the specimen instability [34].

Figure 4 shows the schematic diagrams of the acoustic emission points in the uniaxial loading process which correspond to the final point of each stress-strain curve at day 28 and different substitution rates. The greater the compressive strength, the greater the number of acoustic emission fracture points. For groups C0 and C4, the relatively few fracture points are mostly concentrated on the diagonal face of the CGCAB cube specimen. For groups C1, C2, and C3, many fracture points are concentrated on the central column of the CGCAB cube specimen. Moreover, the failure mode of CGCAB is similar to that of concrete, and two opposite pyramid-shaped fracture surfaces are formed [35, 36]. We observed that the CGCAB law of failure mode was not the same as the concrete one, but it was similar to that of soft rock. These results may be attributed to the hardness of CGCAB, which is closer to soft rock and softer than concrete. The failure mode is a single slope for softer materials and an X-shaped conjugate slope for harder materials [37].

When the substitution rate was 0% or 40%, the hydration and pozzolanic reactions were relatively incomplete at day 28. Moreover, the CGCAB specimens were in a soft state. Thus, their failure mode was closer to a monoclinic fracture (Figures 4(a) and 4(e)). Such CGCAB specimens lose less

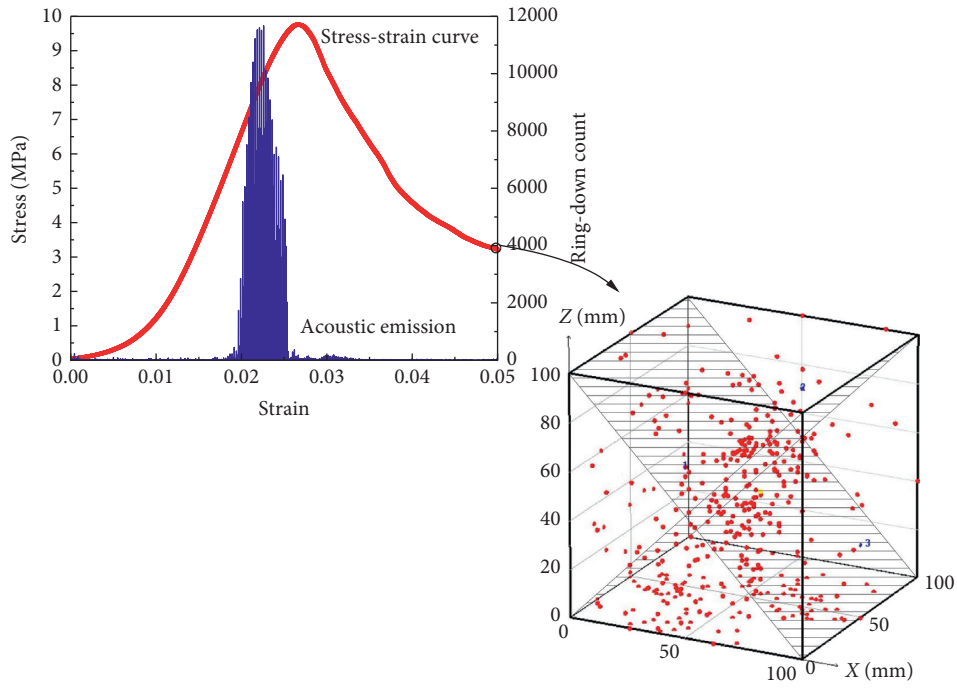


(a)

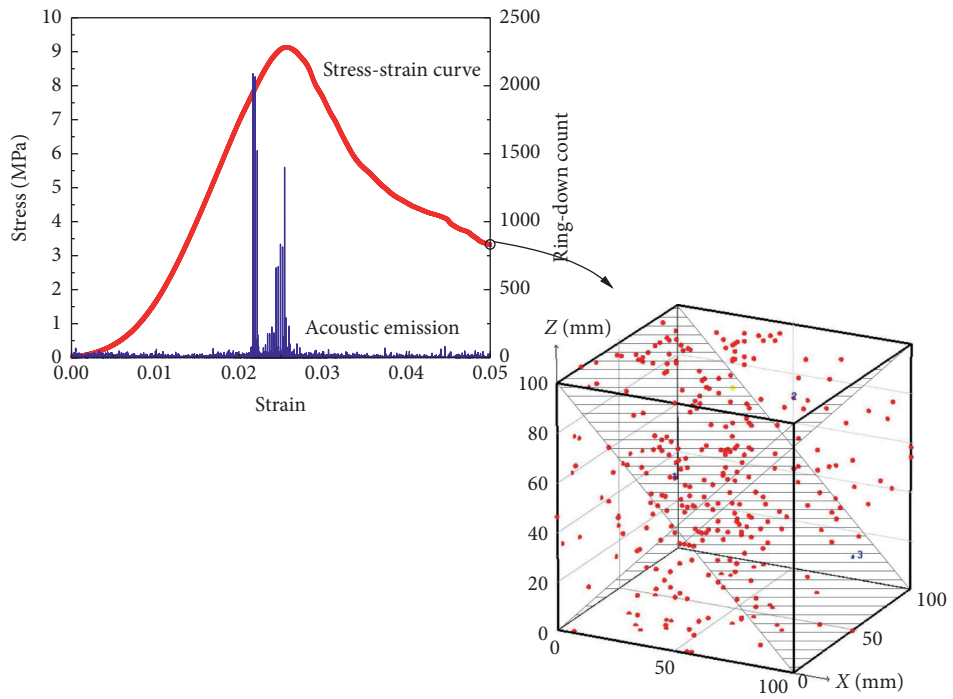


(b)

FIGURE 4: Continued.



(c)



(d)

FIGURE 4: Continued.

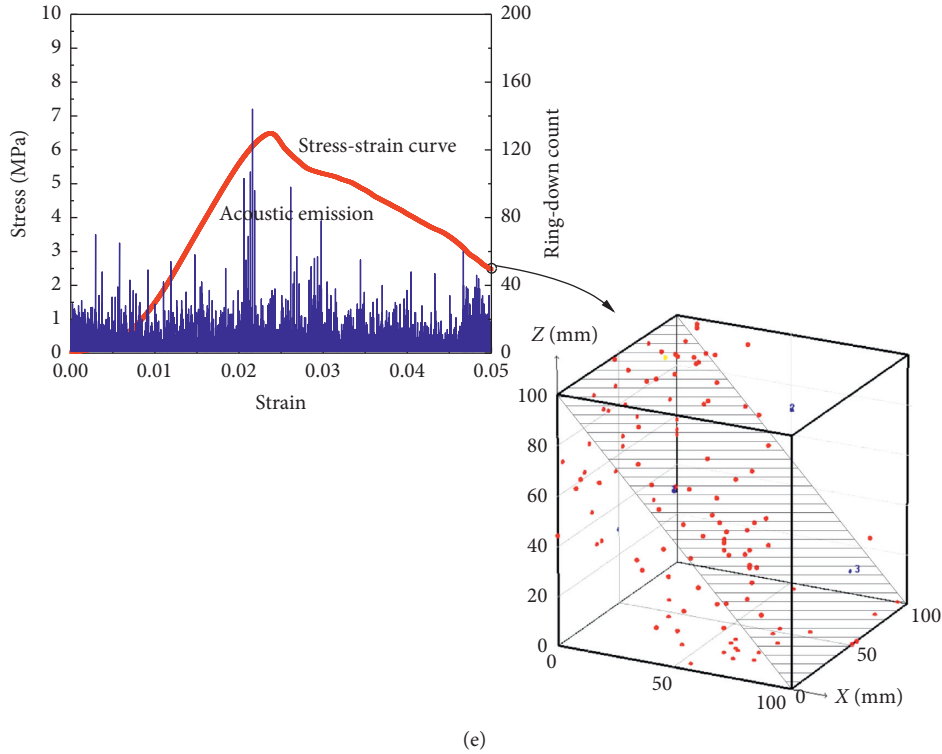


FIGURE 4: Stress-strain-acoustic emission ring-down count and fracture points during uniaxial loading at day 28 with different substitution rates: (a) 0% (C0), (b) 10% (C1), (c) 20% (C2), (d) 30% (C3), and (e) 40% (C4).

energy due to cracking during uniaxial loading than hard specimens for a moderate substitution rate of 10–30%. This conclusion can be confirmed in Figure 5. For group C2, the total amount of energy released by the CGCAB specimen detected by the acoustic emission device was the largest. The final accumulated energy was arranged from highest to lowest in the following order: C2, C3, C1, C0, and C4. At different substitution rates, the energy released during the pore closure stage and reversible elastic deformation stage slightly changed. The stage that causes the accumulated energy to rise sharply is the unstable fracture development stage (yield stage). For 20% or 30% substitution rate, the unstable fracture clearly develops, and the accumulated energy rises sharply. Under other substitution rates, the fracture development is relatively stable, and the accumulated energy rises steadily.

3.3. *Shear Strength.* Considering the analysis of rock, soil, and concrete against shear strength, the Mohr-Coulomb criterion (equation 1) can be used to analyse the shear resistance of CGCAB [38–40].

$$\tau = \sigma \tan \phi + c, \tag{1}$$

where τ is the shear stress on the shear fracture surface (i.e., the shear strength of CGCAB), MPa; σ is the normal stress, MPa; ϕ is the internal friction angle, °; and c is cohesion, MPa.

The axial stress combined with the angle of the shearing fixture is decomposed into normal stress and shear stress

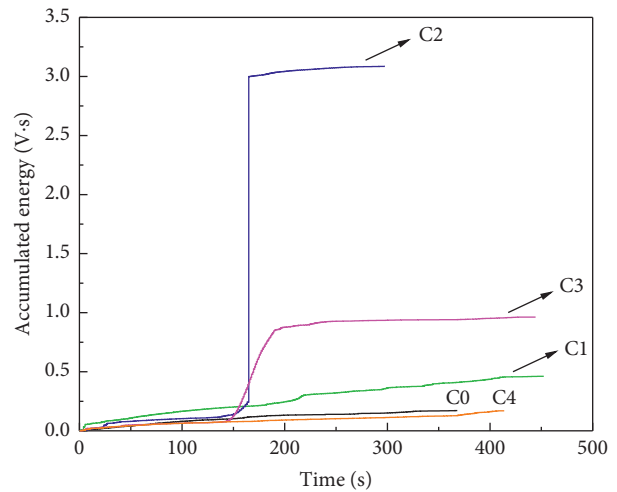


FIGURE 5: Correlation between accumulated energy and loading time at day 28.

(i.e., shear strength). The relationship between the shear strength of different shear angles (40°, 45°, 50°, and 55°) and the substitution rate under the same curing age is shown in Figure 6. At day 3, the shear strength showed a tendency to gradually decrease, and group C0 presented the highest shear strength. At days 7, 14, and 28, the shear strength first increased and then decreased. However, the corresponding substitution rate for the group with the highest shear strength was not the same. At day 7, the corresponding group with the highest shear strength was C1 for the four

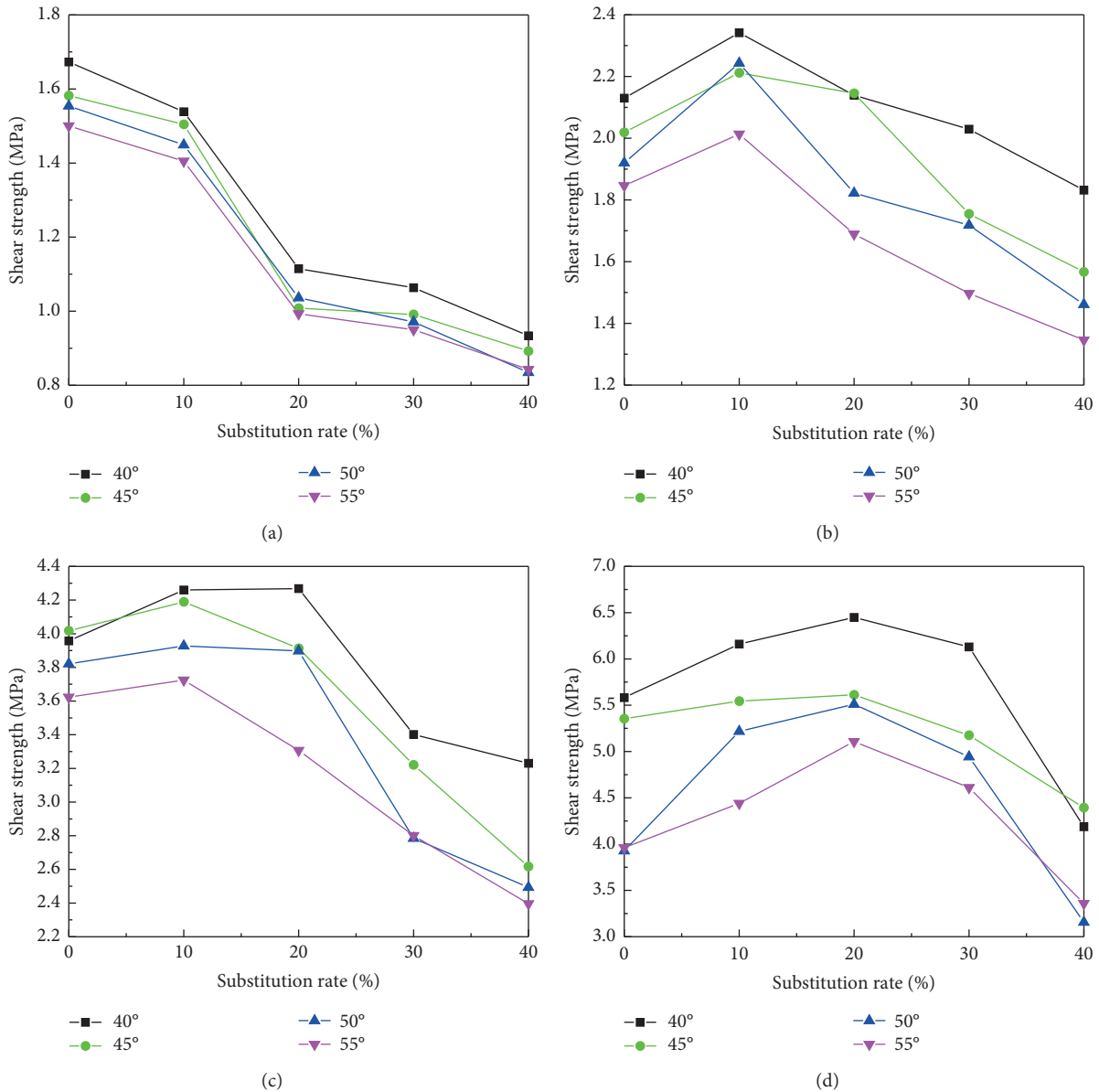
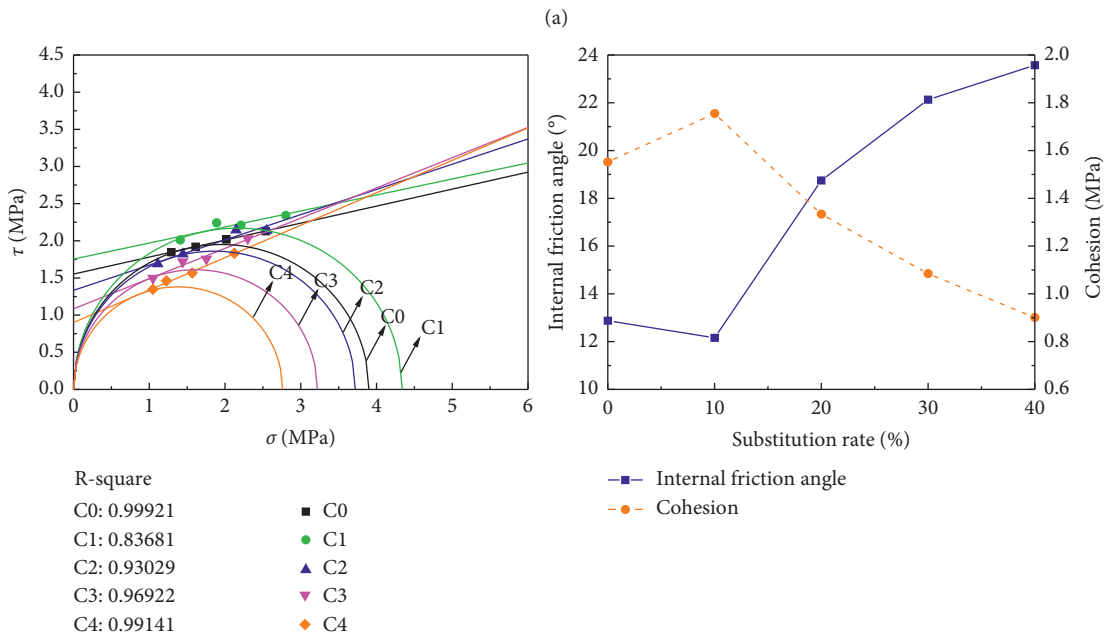
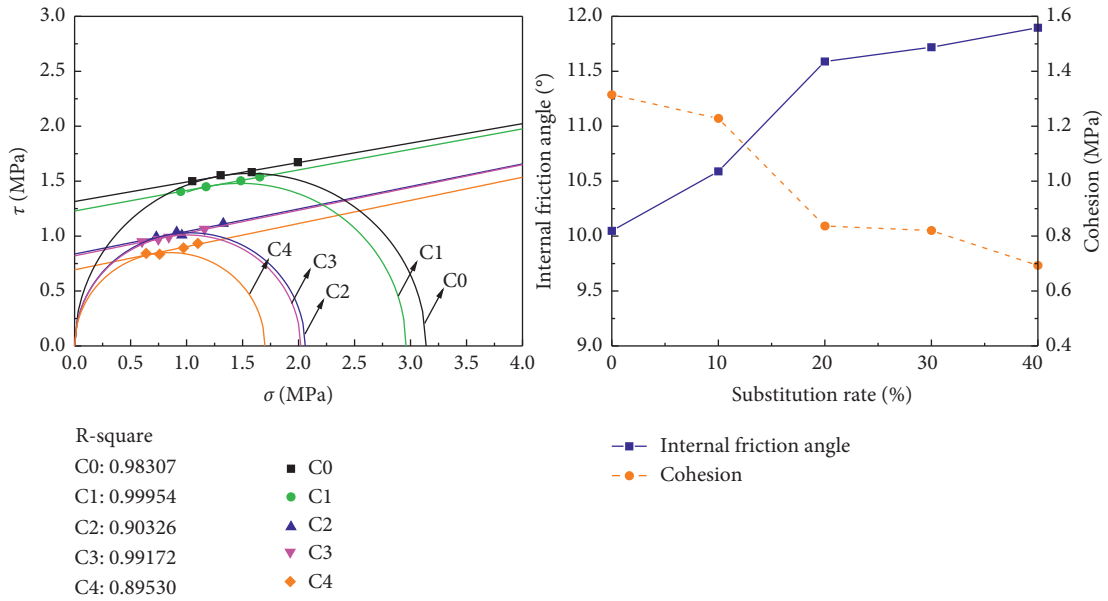


FIGURE 6: Correlation between shear strength and substitution rate at (a) 3, (b) 7, (c) 14, and (d) 28 days of curing age.

shear angles. At day 14, they were C1 for 45°, 50°, or 55° shear angle and C2 for 40° shear angle. At day 28, it was C2 for all four shear angles. The optimal substitution rate gradually changed from 10% to 20% with increasing curing time, which is consistent with the compressive strength results. This behaviour occurs because the internal mechanism of shear strength change is almost the same as the one of compressive strength. It was also observed that, at the same curing age and substitution rate, the shear strength decreases as the shear angle increases. Thus, the higher the shear angle, the higher the portion of axial stress decomposed into normal stress, the lower the portion decomposed into the shear stress, and the smaller the shear strength.

To further explore the relationship between substitution rate and parameters in the shear strength formula

(i.e., the Mohr-Coulomb criterion), the Mohr circle for uniaxial loading was plotted, as shown in Figure 7. The abscissa of the right intersection of the Mohr circle and the horizontal axis is the maximum principal stress value. A similar result (difference of approximately 1 MPa) was obtained for the maximum principal stress on the drawn Mohr circle with compressive strength. This indicates that the Mohr-Coulomb criterion is suitable for evaluating the mechanical properties of CGCAB. For uniaxial loading, the radius represents half of the maximum principal stress in the Mohr circle. At day 3, the radius of the Mohr circle showed a decreasing trend with increasing substitution rate, and the radius of the Mohr circle for group C0 was the largest. At days 7 and 14, the radius of the Mohr circle first increased and then decreased with an increasing substitution rate. The radius of the Mohr circle for group C1 was



(b)
FIGURE 7: Continued.

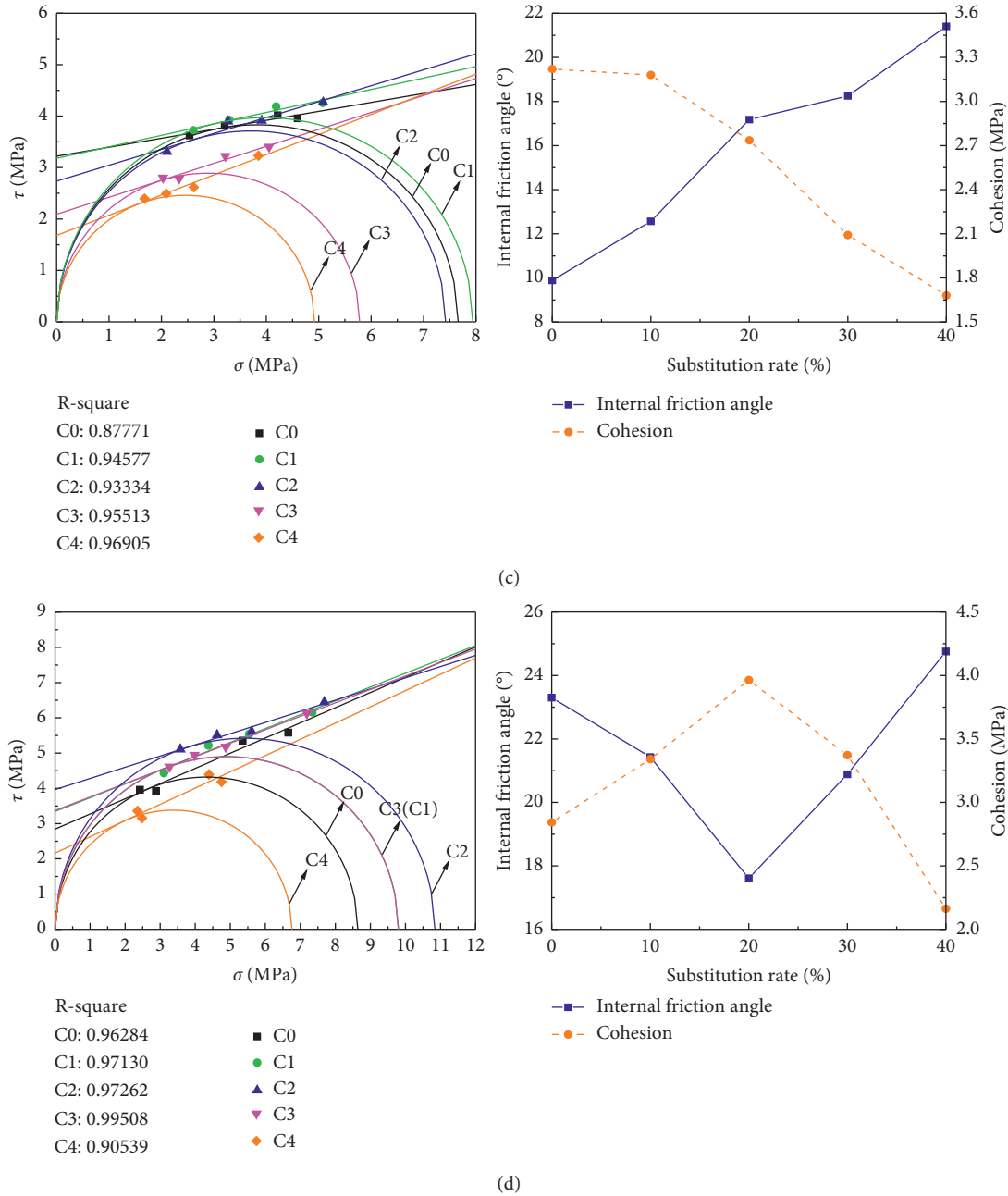


FIGURE 7: Mohr circles and CGCAB parameters at (a) 3, (b) 7, (c) 14, and (d) 28 days of curing age.

the largest. At day 28, the radius of the Mohr circle also presented an increasing trend first and then a decreasing trend upon increasing substitution rate. The radius of the Mohr circle was the largest for group C2. In addition, the relative positions of the various Mohr circles demonstrate that group C2's catch-up momentum is the strongest from medium to large, followed by group C3's. The remaining Mohr circles did not catch up with other Mohr circles but developed stepwise with age.

The tangent line of the Mohr circle is a linear envelope, known as the Mohr-Coulomb failure criterion. Its slope represents the tangent value of the internal friction angle, and its intercept represents the cohesion. These two

important parameters correspond to the friction and cohesive strengths, respectively [41]. Figure 7 shows the internal friction angle and cohesion of CGCAB of various ages as functions of the substitution rate. At days 3 and 14, the internal friction angle gradually increased with increasing substitution rate, and the internal friction angles for group C4 were the largest (11.9° and 21.4° for days 3 and 14, respectively). In contrast, cohesion gradually decreased with increasing substitution rate, and the cohesion values for group C0 were the largest (1.3 MPa and 3.2 MPa for days 3 and 14, respectively). At day 7, the internal friction angle first decreased and then increased with increasing substitution rate. The internal friction angle for group C4 was still

the largest (23.6°). The cohesion first increased and then decreased with increasing substitution rate, and the cohesion for group C1 was the largest (1.8 MPa). At day 28, the trends of internal friction angle and cohesion were the same as the ones from day 7. The internal friction angle for group C4 was still the largest (24.8°), but the largest cohesion was observed for group C2 (4 MPa).

Comparing Figures 3 and 7, it is clear that the greater the compressive strength, the smaller the internal friction angle and the greater the cohesion for identical substitution rate compared to different substitution rates. This behaviour may happen because, after the pozzolanic reaction, the coal gangue is wrapped into a regular ellipsoid. Thus, the friction strength of the specimen is easily reduced with increasing substitution rate, whereas the cementation force increases with increasing C-S-H content, so that the cohesive strength of the specimen also increases with the increasing substitution rate. However, with the gradual increase of substitution rate, the change in workability hinders the maintenance of the pozzolanic reaction. Thus, the internal friction angle increases and the cohesion decreases. According to the acoustic emission fracture points (Figure 4), failure is mainly attributed to the shear of specimen, and the axial stress is transformed into normal and shear stress on the surface of the shear fracture. In the loading of CGCAB, both shearing and compression are possible, but it is not possible to consider only one of them.

3.4. Drying Shrinkage. The drying shrinkage performance of CGCAB is related to an important quality index in the backfilling mining process: the rate of supporting pit roof. The larger the drying shrinkage is, the smaller the rate of supporting pit roof is and the more difficult it is for the CGCAB to meet the roof of the roadway during the actual backfilling process. Consequently, ground collapse is more likely to occur. The drying shrinkage of CGCAB at different ages (days 1, 3, 7, 14, 28, 45, 60, 90, 120, and 180) with different substitution rates is shown in Figure 8. It can be seen that the drying shrinkage increases with extended age due to the loss of water inside the specimen [42]. This loss can be attributed to the evaporation of internal water and the consumption of water by chemical reactions [43].

CGCAB specimens under natural dry conditions shrank faster from days 3 to 7 in this study. Thus, the chemical reaction rate was the fastest in that period, which was the key stage for strength development. For group C2, CGCAB presented the largest drying shrinkage after 3 days. For 20% substitution rate, the hydration and pozzolanic reactions in the CGCAB are thoroughly performed, so they consume the most water and produce the most C-S-H colloids. When the substitution rate is too small or too large, these reactions are inhibited by the shortage of CSFA or free water. Thus, less water is consumed, and the drying shrinkage is lower than when the

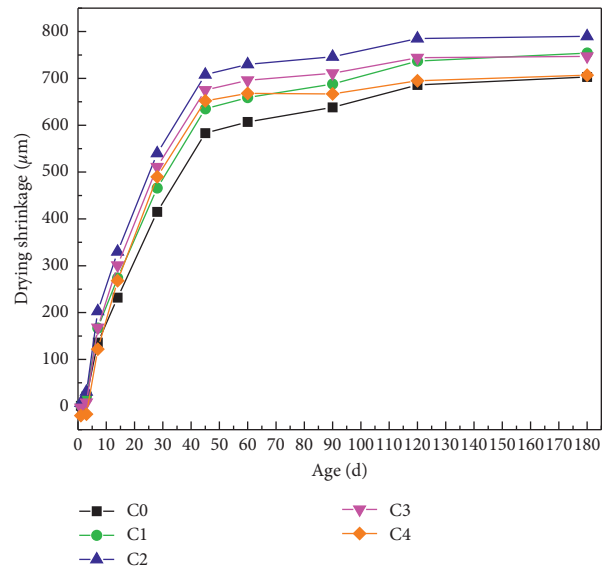


FIGURE 8: CGCAB drying shrinkage trend.

substitution rate was 20%. In addition, it can be seen that, at 180 days, the drying shrinkages of C0 and C4 groups are almost equal, while C1 and C3 groups are also close. This indicates that the addition of CSFA can accelerate the completion of drying shrinkage. This may be related to the porous nature and coarse morphology of the CSFA particles.

3.5. Microscopic Analysis. To corroborate the mechanism analyses of the above subsections and ensure that they can be tested by practice, SEM images of CGCAB under different substitution rates at day 28 were obtained. As shown in Figure 9, C-S-H is produced in a fibrillar morphology [44]. The highest C-S-H production was observed for group C2. When CSFA was not added, C-S-H was distributed in a relatively dispersed form among the individual particles. For 20% CSFA, C-S-H was clearly concentrated in a large agglomerate shape and acted as a bridge connection between the particles. For 40% CSFA, the concentration of C-S-H was significantly weakened, and many particles were not covered by C-S-H. This behaviour likely occurred because their pozzolanic activity could not be exerted in a water-deficient environment. Moreover, for low cement content, the amount of calcium hydroxide formed by cement hydration was relatively small, and the degree of pozzolanic reaction was relatively low. Consequently, the reaction product formed was relatively small. Microscopic analysis establishes a similar relationship to mechanical properties. There is a positive correlation between mechanical strength and C-S-H content. With the increase of C-S-H content, the CGCAB is denser, and the compressive strength, acoustic emission energy, and shear strength are generally higher. These SEM images further confirm that 20% is the best substitution rate for CSFA to replace cement in CGCAB.

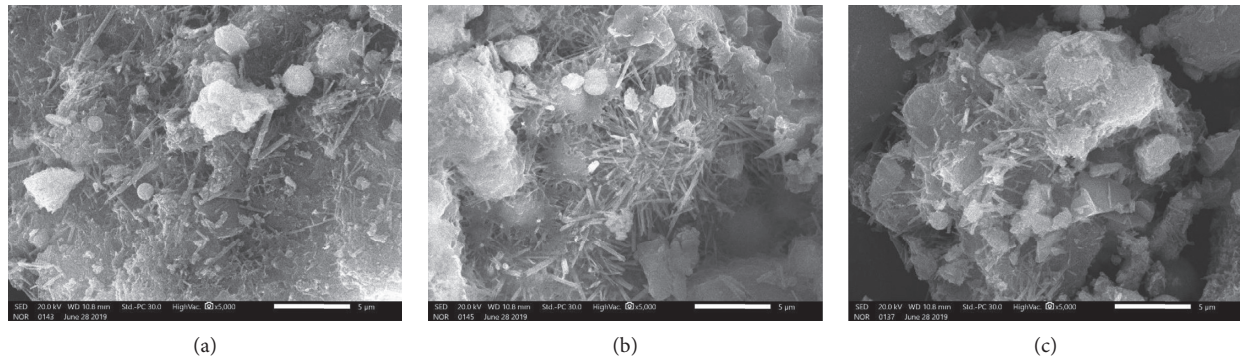


FIGURE 9: SEM images of CGCAB at day 28 and (a) 0% (C0), (b) 20% (C2), and (c) 40% (C4) substitution rates.

4. Conclusion

In this study, the cement in CCGB was replaced by CSFA at 0, 10, 20, 30, and 40 wt%, and the effects on the mechanical and deformation properties of CGCAB, including compressive strength, shear strength, stress-strain-acoustic emission, and drying shrinkage, were analysed. The compressive and shear strength tests were performed at the curing age of 3, 7, 14, and 28 days. The acoustic emission test was performed only for day 28. The drying shrinkage test was performed at days 1, 3, 7, 14, 28, 45, 60, 90, 120, and 180. The main conclusions are summarized as follows:

- (1) At days 3, 7, and 14, the group with a 10% substitution rate showed the highest compressive strength. However, by day 28, the group with a 20% substitution rate presented the highest compressive strength. The peak of acoustic emission ring-down count was observed mainly in the unstable fracture development stage (yield stage) before the stress peak and after the yield point. When the substitution rate was 20%, the peak was the highest, and the amount of accumulated energy was the largest at day 28. In that same day, the failure mode was similar to two opposite pyramid-shaped fractures for substitution rate between 10% and 30%, whereas, for 0% or 40%, the failure mode was closer to a monoclinical fracture. It was observed in the SEM images that the calcium silicate hydrates in CGCAB have a fibrillar morphology and are mostly generated when the substitution rate was 20%.
- (2) At day 3, the shear strength showed a tendency to gradually decrease, and the group with a substitution rate of 0% presented the highest shear strength. At days 7, 14, and 28, the shear strength first increased and then decreased. However, the corresponding substitution rate for the group with the highest shear strength was different (gradual transition from 10% to 20%). The Mohr-Coulomb criterion was applied to the shear strength test analysis of CGCAB. At days 3 and 14, the internal friction angle gradually increased, while the cohesion gradually decreased. At days 7 and 28, the internal friction angle first decreased and then increased, whereas the cohesion

first increased and then decreased. In terms of shear strength, a 20% CSFA substitution rate is recommended for suitable internal friction angles and cohesion.

- (3) The drying shrinkage increased with extended age, and the fastest shrinking rates of CGCAB under natural dry conditions occurred from day 3 to day 7. The group with a substitution rate of 20% presented the largest drying shrinkage at any age. The addition of CSFA can accelerate the completion of drying shrinkage.

Data Availability

The data used to support the findings of this study are included within the article.

Conflicts of Interest

The authors declare that they have no conflicts of interest.

Acknowledgments

This work was supported by the Joint Research Fund under a cooperative agreement between the NSFC and Funds for Coal-Based Low-Carbon Technology of Shanxi (nos. U1710258 and U1810120); the National Natural Science Foundation of China (nos. 51574172 and 51804208); the Key Research and Development Program (Social Development) of Shanxi Province (201803D31044); the Research Fund of the State Key Laboratory of Coal Resources and Safe Mining, CUMT (SKLRCRSM18KF016); and the China Postdoctoral Science Foundation (2018M632423). Thanks are due to all who supported this basic research.

References

- [1] X. X. Miao and M. G. Qian, "Research on green mining of coal resources in China: current status and future prospects," *Journal of Mining and Safety Engineering*, vol. 26, no. 1, pp. 1–14, 2009.
- [2] X. J. Zhu, G. L. Guo, J. F. Zha, T. Chen, Q. Fang, and X. Y. Yang, "Surface dynamic subsidence prediction model of solid backfill mining," *Environmental Earth Sciences*, vol. 75, no. 12, p. 1007, 2016.

- [3] M. Fall and M. Pokharel, "Coupled effects of sulphate and temperature on the strength development of cemented tailings backfills: portland cement-paste backfill," *Cement and Concrete Composites*, vol. 32, no. 10, pp. 819–828, 2010.
- [4] M. Helinski, M. Fahey, and A. Fourie, "Coupled two-dimensional finite element modelling of mine backfilling with cemented tailings," *Canadian Geotechnical Journal*, vol. 47, no. 11, pp. 1187–1200, 2010.
- [5] J. Huazhe, W. Shufei, Y. Yixuan, and X. Chen, "Water recovery improvement by shearing of gravity-thickened tailings for cemented paste backfill," *Journal of Cleaner Production*, vol. 245, p. 118882, 2020.
- [6] Y. Feng, Q. Yang, Q. Chen et al., "Characterization and evaluation of the pozzolanic activity of granulated copper slag modified with cao," *Journal of Cleaner Production*, vol. 232, pp. 1112–1120, 2019.
- [7] P.-M. Wang and X.-P. Liu, "Effect of temperature on the hydration process and strength development in blends of portland cement and activated coal gangue or fly ash," *Journal of Zhejiang University-SCIENCE A*, vol. 12, no. 2, pp. 162–170, 2011.
- [8] D. Wu, S.-J. Cai, and Y.-C. Liu, "Effects of binder on suction in cemented gangue backfill," *Magazine of Concrete Research*, vol. 68, no. 12, pp. 593–603, 2016.
- [9] D. Wu, T. Deng, and R. Zhao, "A coupled thmc modeling application of cemented coal gangue-fly ash backfill," *Construction and Building Materials*, vol. 158, pp. 326–336, 2018.
- [10] B. Yin, T. Kang, J. Kang, and Y. Chen, "Experimental and mechanistic research on enhancing the strength and deformation characteristics of fly-ash-cemented filling materials modified by electrochemical treatment," *Energy & Fuels*, vol. 32, no. 3, pp. 3614–3626, 2018.
- [11] Q. Sun, B. Li, S. Tian, C. Cai, and Y. Xia, "Creep properties of geopolymer cemented coal gangue-fly ash backfill under dynamic disturbance," *Construction and Building Materials*, vol. 191, pp. 644–654, 2018.
- [12] H.-Z. Jiao, S.-F. Wang, A.-X. Wu, H.-M. Shen, and J.-D. Wang, "Cementitious property of naalo₂-activated ge slag as cement supplement," *International Journal of Minerals, Metallurgy and Materials*, vol. 26, no. 12, pp. 1594–1603, 2019.
- [13] Y. He, Q. Chen, C. Qi, Q. Zhang, and C. Xiao, "Lithium slag and fly ash-based binder for cemented fine tailings backfill," *Journal of Environmental Management*, vol. 248, Article ID 109282, , 2019.
- [14] Q.-S. Chen, Q.-L. Zhang, A. Fourie, X. Chen, and C.-C. Qi, "Experimental investigation on the strength characteristics of cement paste backfill in a similar stope model and its mechanism," *Construction and Building Materials*, vol. 154, pp. 34–43, 2017.
- [15] Y. Bi, C. Gao, Y. Wang, and B. Li, "Estimation of straw resources in China," *Transactions of the CSAE*, vol. 25, no. 12, pp. 211–217, 2009.
- [16] Z. Wang, T. Lei, M. Yang et al., "Life cycle environmental impacts of cornstalk briquette fuel in China," *Applied Energy*, vol. 192, pp. 83–94, 2017.
- [17] G. R. Feng, T. Y. Qi, Z. H. Wang, J. W. Bai, and Z. Li, "Physical and chemical characterization of Chinese maize stalk leaf ash: calcining temperature and aqueous solution," *Bioresources*, vol. 14, no. 1, pp. 977–995, 2019.
- [18] G. G. Kaya, E. Yilmaz, and H. Deveci, "Sustainable nanocomposites of epoxy and silica xerogel synthesized from corn stalk ash: enhanced thermal and acoustic insulation performance," *Composites Part B: Engineering*, vol. 150, pp. 1–6, 2018.
- [19] R. K. Sandhu and R. Siddique, "Influence of rice husk ash (rha) on the properties of self-compacting concrete: a review," *Construction And Building Materials*, vol. 153, pp. 751–764, 2017.
- [20] A. N. Givi, S. A. Rashid, F. N. A. Aziz, and M. A. M. Salleh, "Assessment of the effects of rice husk ash particle size on strength, water permeability and workability of binary blended concrete," *Construction and Building Materials*, vol. 24, no. 11, pp. 2145–2150, 2010.
- [21] M. R. Elias, V. A. Javad, and D. M. Reza, "Mechanical performance of self-compacting concrete incorporating rice husk ash," *Construction and Building Materials*, vol. 177, pp. 148–157, 2018.
- [22] C. Fapohunda, B. Akinbile, and S. Ahmed, "Structure and properties of mortar and concrete with rice husk ash as partial replacement of ordinary Portland cement-a review," *International Journal of Sustainable Built Environment*, vol. 6, no. 2, pp. 675–692, 2017.
- [23] R. Madandoust, M. M. Ranjbar, H. A. Moghadam, and S. Y. Mousavi, "Mechanical properties and durability assessment of rice husk ash concrete," *Biosystems Engineering*, vol. 110, no. 2, pp. 144–152, 2011.
- [24] N. Van Tuan, G. Ye, K. van Breugel, and O. Copuroglu, "Hydration and microstructure of ultra high performance concrete incorporating rice husk ash," *Cement and Concrete Research*, vol. 41, no. 11, pp. 1104–1111, 2011.
- [25] M. S. Ismail and A. M. Waliuddin, "Effect of rice husk ash on high strength concrete," *Construction and Building Materials*, vol. 10, no. 7, pp. 521–526, 1996.
- [26] F. A. Olutoge and P. A. Adesina, "Effects of rice husk ash prepared from charcoal-powered incinerator on the strength and durability properties of concrete," *Construction and Building Materials*, vol. 196, pp. 386–394, 2019.
- [27] X. Du, G. Feng, Y. Zhang, Z. Wang, Y. Guo, and T. Qi, "Bearing mechanism and stability monitoring of cemented gangue-fly ash backfill column with stirrups in partial backfill engineering," *Engineering Structures*, vol. 188, pp. 603–612, 2019.
- [28] T. Sinsiri, W. Kroehong, C. Jaturapitakkul, and P. Chindaprasit, "Assessing the effect of biomass ashes with different finenesses on the compressive strength of blended cement paste," *Materials & Design*, vol. 42, pp. 424–433, 2012.
- [29] T. Zhang, H. Chen, X. Li, and Z. Zhu, "Hydration behavior of magnesium potassium phosphate cement and stability analysis of its hydration products through thermodynamic modeling," *Cement and Concrete Research*, vol. 98, pp. 101–110, 2017.
- [30] S. M. S. Kazmi, M. J. Munir, P. Indubhushan, and Y.-F. Wu, "Pozzolanic reaction of sugarcane bagasse ash and its role in controlling alkali silica reaction," *Construction and Building Materials*, vol. 148, pp. 231–240, 2017.
- [31] A. K. Parande, K. Stalin, R. K. Thangarajan, and M. S. Karthikeyan, "Utilization of agrosresidual waste in effective blending in portland cement," *ISRN Civil Engineering*, vol. 2011, pp. 1–12, 2011.
- [32] I. G. Richardson, "Tobermorite/jennite- and tobermorite/calcium hydroxide-based models for the structure of C-S-H: applicability to hardened pastes of tricalcium silicate, β -dicalcium silicate, Portland cement, and blends of Portland cement with blast-furnace slag, metakaolin, or silica fume," *Cement and Concrete Research*, vol. 34, no. 9, pp. 1733–1777, 2004.
- [33] L. Zhang, K. Yamauchi, Z. Li, X. Zhang, H. Ma, and S. Ge, "Novel understanding of calcium silicate hydrate from dilute

- hydration,” *Cement and Concrete Research*, vol. 99, pp. 95–105, 2017.
- [34] T. Qi and G. Feng, “Resistivity and ae response characteristics in the failure process of cgb under uniaxial loading,” *Advances In Materials Science And Engineering*, vol. 2017, Article ID 7857590, 11 pages, 2017.
- [35] S. Cao, E. Yilmaz, W. Song, E. Yilmaz, and G. Xue, “Loading rate effect on uniaxial compressive strength behavior and acoustic emission properties of cemented tailings backfill,” *Construction and Building Materials*, vol. 213, pp. 313–324, 2019.
- [36] G. Feng, X. Du, and Y. Zhang, ““Optical-acoustic-stress” responses in failure progress of cemented gangue-fly ash backfill material under uniaxial compression,” *Nondestructive Testing and Evaluation*, vol. 34, no. 2, pp. 135–146, 2019.
- [37] T. Szwedzicki, “A hypothesis on modes of failure of rock samples tested in uniaxial compression,” *Rock Mechanics and Rock Engineering*, vol. 40, no. 1, pp. 97–104, 2006.
- [38] D. A. Moran and C. P. Pantelides, “Elliptical and circular FRP-confined concrete sections: a Mohr-Coulomb analytical model,” *International Journal of Solids and Structures*, vol. 49, no. 6, pp. 881–898, 2012.
- [39] D. A. Moran, C. P. Pantelides, and L. D. Reaveley, “Mohr-coulomb model for rectangular and square frp-confined concrete,” *Composite Structures*, vol. 209, pp. 889–904, 2019.
- [40] L.-S. Tang, H.-T. Sang, J. Song, Z.-G. Luo, and Y.-L. Sun, “Mechanical model for failure modes of rock and soil under compression,” *Transactions of Nonferrous Metals Society of China*, vol. 26, no. 10, pp. 2711–2723, 2016.
- [41] D. He, W. Yang, and Y. Cheng, “Surface morphology of structural plane and effects of the shear strength parameters,” *Advances in Civil Engineering*, vol. 2018, pp. 1–7, 2018.
- [42] J. Yang, Q. Wang, and Y. Zhou, “Influence of curing time on the drying shrinkage of concretes with different binders and water-to-binder ratios,” *Advances in Materials Science and Engineering*, vol. 2017, Article ID 2695435, 10 pages, 2017.
- [43] J. Li and Y. Yao, “A study on creep and drying shrinkage of high performance concrete,” *Cement and Concrete Research*, vol. 31, no. 8, pp. 1203–1206, 2001.
- [44] I. G. Richardson, “The calcium silicate hydrates,” *Cement and Concrete Research*, vol. 38, no. 2, pp. 137–158, 2008.